analytical chemistry

pubs.acs.org/ac Article

From Static Scaffolds to Dynamic Highways: Spatially Ordered Nanotube Tracks Improve Pathway Control and Accelerate DNA Walker Kinetics for Enhanced MicroRNA Detection

Yongli Wu, Xin Chang, Zhuoxin Ye, Ruixin Liu, Yan Zhang, Ruiyan Liu, Pinyi Ma,* and Daqian Song*

Cite This: Anal. Chem. 2025, 97, 24232−24241 Read Online

ACCESS | Metrics & More | Article Recommendations | SI Supporting Information

ABSTRACT: DNA walkers are programmable molecular machines whose performance depends on the structural precision and spatial organization of their walking tracks. This study presents a rigid and highly ordered DNA nanotube-based track (H-DNT), consisting of periodic anchoring sites spaced 7 nm apart, constructed via the precise self-assembly of single-stranded tiles. Compared to conventional double-stranded or nanosheet DNA tracks, H-DNT significantly improved path controllability and accelerated reaction kinetics, reducing the equilibrium time to only 30 min. By tuning both track length and intertrack spacing, we were able to substantially improve walker motility and signal amplification efficiency. As a proof of concept, the H-DNT system was integrated into an electrochemiluminescence (ECL) biosensing platform for the ultrasensitive detection of microRNA-221 at a concentration as low as 2.42 aM. The platform also had excellent selectivity and stability. This programmable nanodevice provides a robust and generalizable solution for constructing high-performance DNA walker systems, opening new avenues for rapid and sensitive tumor biomarker detection.

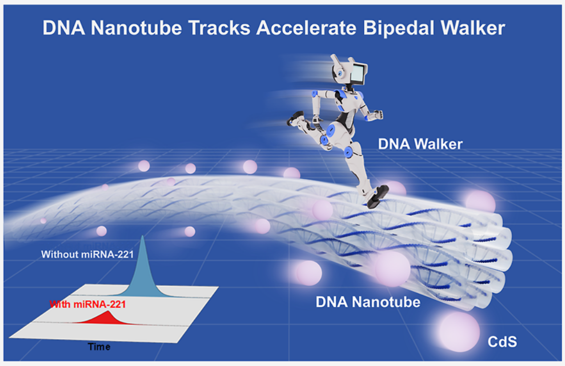

1. INTRODUCTION

DNA walkers are programmable molecular machines capable of autonomous, stepwise movement along predefined tracks.[1,2] Their ability to convert molecular recognition into directional mechanical motion has enabled diverse applications in biosensing,[3] nanomedicine,[4,5] and molecular computation.[6] However, the performance of DNA walkers remains intrinsically constrained by the structural precision and spatial organization of their walking substrates. Conventional DNA tracks, such as double-stranded scaffolds or two dimensional assemblies,[7−10] often suffer from spatial disorder, discontinuous anchoring sites, and limited control over track geometry. These factors lead to inefficient walker movement, frequent derailment, and low signal amplification efficiency. Moreover, nanoscale challenges, such as nonuniform molecular spacing, steric interference, and trade-offs in strand concentration, further compromise the robustness and dynamic control of the system.[11−13]

To overcome these limitations, recent efforts have focused on the structural engineering of DNA nanomaterials.[14] Owing to their highly programmable base-pairing interactions, DNA nanostructures can be precisely designed to form spatially addressable frameworks with nanoscale resolution.[15−18] Among these, rigid linear DNA architectures offer the potential to guide directional walker motion through periodic anchoring and sterically optimized pathways.[19] We have previously developed a sensing platform based on positively charged carbon dot-mediated DNA triangular prism frameworks.[20] The use of spatially ordered linear-stepped DNA tracks significantly improves sensing efficiency. Although this track-ordering design enhances the walker's motility and signal amplification to some extent, the system still faces critical technical challenges, including discontinuous movement caused by intermodular steric hindrance effects, which limit further improvement of overall system performance. Therefore, a generalizable track system that combines long-range order, tunable parameters, and high mechanical integrity remains elusive.

MicroRNAs (miRNAs), a class of short noncoding RNAs, have emerged as promising biomarkers for cancer diagnosis, classification, and prognosis.[21,22] However, their low abundance in clinical samples poses a significant analytical challenge.[23,24] DNA walker-based biosensing platforms offer an effective strategy for signal amplification and target recognition in miRNA detection in ultrasensitive and noninvasive analysis.[25,26] Among various cancer related miRNAs, miRNA-221 is closely associated with hepatocellular carcino-

Received: August 27, 2025
Revised: October 8, 2025
Accepted: October 20, 2025
Published: October 22, 2025

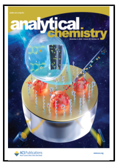

https://doi.org/10.1021/acs.analchem.5c05240
Anal. Chem. 2025, 97, 24232−24241

Scheme 1. Schematic Diagram of the Biosensing Platform for Detecting miRNA-221[a]

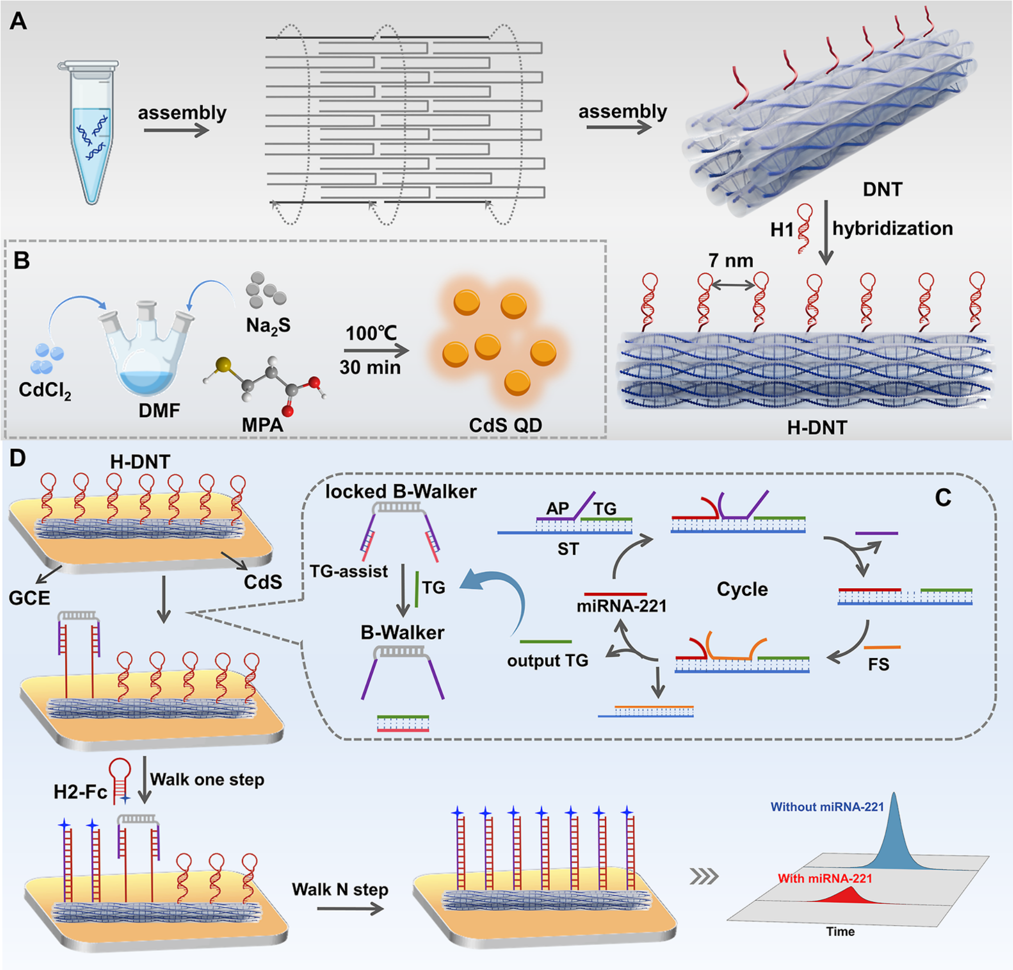

[a](A) Assembly of the DNA nanotube by single-stranded tiles as DNA tracks. (B) Synthesis of CdS QDs. (C) Conversion of target miRNA-221 to TG via strand displacement reaction, which activates the B-walker. (D) Construction of the electrochemical biosensor for miRNA-221 detection.

ma;[27] thus, it can serve as a valuable model for validating the analytical capabilities of novel biosensing systems.

In this study, we designed and fabricated a micrometer-scale DNA nanotube track (H-DNT) via single-stranded tile assembly. This rigid and spatially ordered track, consisting of anchoring sites arranged precisely 7 nm apart, provides a highly directional and continuous path for bipedal DNA walkers (B-walkers). By systematically tuning the track length and intertrack spacing, we improved walker motility and signal amplification efficiency. Leveraging the programmability of DNA architecture, the H-DNT system addresses key limitations of conventional track designs by enhancing path controllability and reducing stochastic diffusion. The platform was successfully employed in electrochemiluminescence (ECL) detection of miRNA-221, which demonstrates its practical applicability, highlighting its potential for constructing other robust and adaptable molecular sensing systems.

2. EXPERIMENTAL SECTION

2.1. Synthesis of CdS Quantum Dots (QDs). CdS QDs were synthesized via a modified aqueous-phase method.[28] Briefly, 1 mmol of CdCl$_2$ and 1.7 mmol of mercaptopropionic acid (MPA) were dissolved in 20 mL of deionized water, and the pH of the mixture was adjusted to ~10 using NaOH. The precursor solution was transferred to a three-neck flask. Under continuous nitrogen flow and vigorous stirring, 5 mL of Na$_2$S solution (0.2 M) was added dropwise. The mixture was refluxed at 100 °C for 30 min. A transparent yellow solution was used as an indicator for the successful formation of CdS QDs. The QDs were purified via ethanol precipitation by centrifugation at 4000*g* for 5 min, and this step was repeated 3 times. The product was collected, vacuum-dried at 60 °C, and then redispersed in ultrapure water for further use.

2.2. Assembly of the Bipedal DNA Walker (B-Walker). The B-walker was assembled in a locked conformation using thermal annealing. Probe 1 and Probe 2 strands were mixed with a blocking strand (TG-assist) at a molar ratio of 1:1:2 in Tris-acetate buffer. The mixture was heated to 95 °C for 10 min to denature secondary structures, then gradually cooled to 25 °C for 2 h to allow hybridization and self-assembly into the locked walker complex. To activate the B-walker, TG strands generated via a strand displacement reaction were added to the preassembled system. The TG strand displaced TG-assist via competitive binding, releasing the walker into its functional state and enabling subsequent target-induced motion.

2.3. Assembly of DNA Nanotube Tracks (H-DNT). H-DNT was assembled using thermal annealing. All oligonucleotides were mixed at a final concentration of 1 μM in folding buffer containing 10 mM Tris−HCl and 12 mM MgCl$_2$ (pH

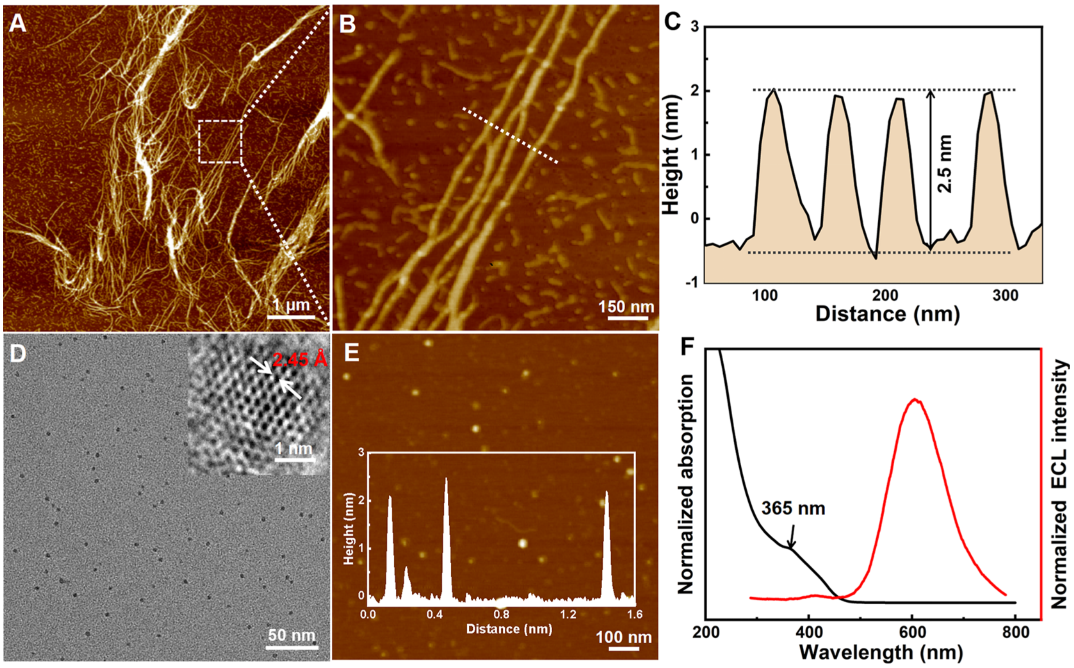

Figure 1. Structural and optical characterization of the DNA nanotubes and CdS QDs. AFM analysis of DNA nanotubes. (A) Low-magnification and (B) high-resolution topographic images. (C) The corresponding cross-sectional height profile, measured along the white dashed line in (B). (D) TEM and (E) AFM image of CdS QDs (inset: a high-resolution TEM image of CdS QDs). (F) UV−visible absorption and ECL spectra of CdS QDs.

8.0). The solution was heated at 95 °C for 10 min to denature strands, then gradually cooled to 25 °C at a rate of 1.5 °C/min to promote ordered self-assembly. Subsequently, H1 hairpin probes were added to the assembled nanotubes and incubated at 37 °C for 2 h to allow site-specific hybridization onto the anchoring domains. To remove excess single strands and unassembled components, the mixture was purified using 100 kDa Amicon Ultra 0.5 mL centrifugal filters (Millipore) through three cycles of centrifugation at 10,000*g* for 6 min. The buffer volume was replenished between cycles to maintain sample integrity. The final concentration of purified H-DNT was determined by measuring UV absorbance at 260 nm.

2.4. Construction of the Electrochemical Biosensor.

The electrochemical biosensor was constructed using a glassy carbon electrode (GCE) via stepwise surface modification. The GCE was first polished with 0.05 μm alumina slurry and then ultrasonically cleaned with deionized water and ethanol to ensure surface cleanliness. A uniform layer of CdS QDs was formed by drop-casting the purified QD solution onto the cleaned electrode, followed by air drying at room temperature. Subsequently, 10 μL of thiol-modified, preassembled H-DNT solution was applied to the CdS-modified electrode and incubated at 4 °C for 12 h to form Cd−S bonds. Unbound nanotubes were removed by rinsing the electrode 3 times with PBS (pH 7.4). To complete the sensing interface, 5 μL of B-walker solution was mixed with an equal volume of 2.0 μM ferrocene-labeled H2 probe solution and incubated with the electrode at 37 °C for 1 h. This coimmobilization step allowed for activation of the walking mechanism and integration of the electrochemical signal transduction components.

3. RESULTS AND DISCUSSION

3.1. Principle of the Biosensing Strategy.

To address limitations of conventional DNA walker tracks, such as structural discontinuity, probe entanglement, and steric hindrance, we employed DNA nanotechnology to construct a rigid and spatially ordered scaffold. As illustrated in Scheme 1A, a 10-helix DNA nanotube (DNT) was assembled using a single-stranded tile (SST) strategy.[29,30] The nanostructure was formed from ten custom-designed 42-nucleotide oligonucleotides, each containing four short binding domains (10−11 nt), which self-assembled into ten parallel double helices with high precision. For functionalization, a thiol group was introduced at the 3′-terminus of the U1 subunit to allow covalent anchoring onto the electrode surface. Additionally, a 15 nt extension with defined 7 nm spacing was incorporated into the U1 sequence to facilitate the periodic and precise hybridization of H1 hairpin probes on the nanotube surface to form the conjugate (H-DNT), The design schematic is shown in Figure S1. This design in this modular and programmable platform can be employed for building structurally precise molecular devices.

Building on this DNA nanomachines, we constructed a novel ECL biosensing platform for miRNA-221 detection. As shown in Scheme 1B, CdS QDs were synthesized to serve as stable luminescent emitters. A locked bipedal DNA walker (B-walker) was assembled from three DNA strands (Scheme 1C, Figure S2). In the presence of miRNA-221, a strand displacement reaction (SDR) generates a trigger strand (TG) that specifically activates the B-walker, allowing it to move along the H-DNT track. For sensor fabrication (Scheme 1D), H-DNT was covalently immobilized onto a CdS-modified glassy carbon electrode (CdS/GCE), resulting in an initial "signal-on" state. Upon activation, the B-walker interacts with the H1 hairpin probe array on the nanotube, inducing conformational switching that exposes target-binding domains. These domains subsequently hybridize with ferrocene-labeled H2 probes via toehold-mediated strand displacement, switching the signal from "on" to "off" while releasing the B-walker to continue its motion. This directional, iterative movement

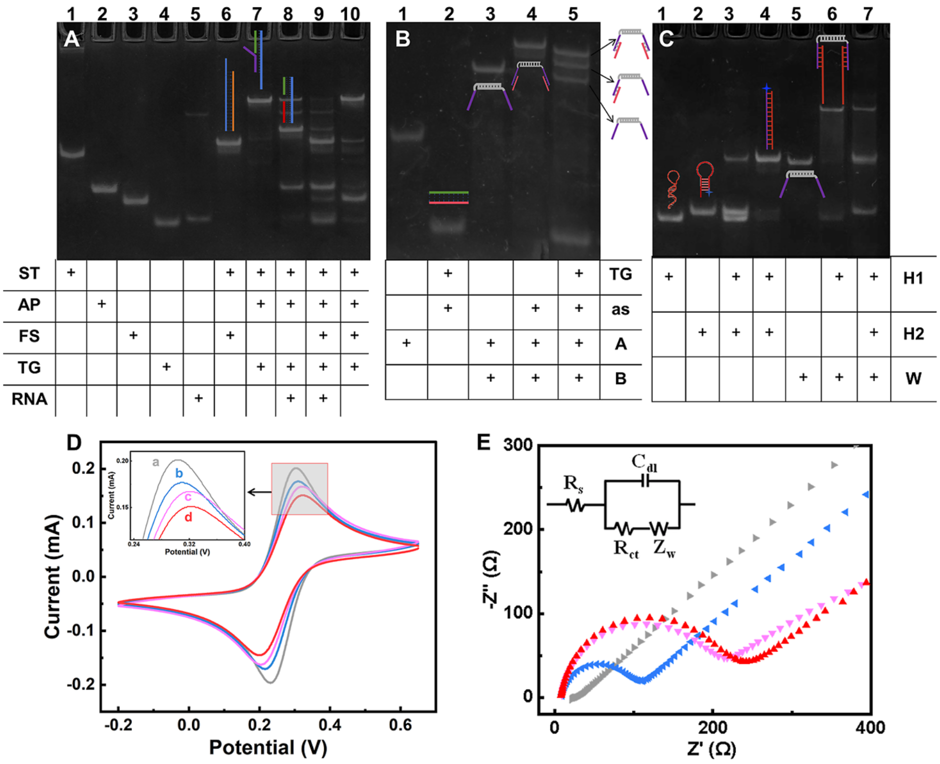

Figure 2. Verify the feasibility of the B-walker strategy and the successful fabrication of the biosensing interface. (A) Native PAGE of strand displacement reaction. (B) Native PAGE of B-walker activation. (C) Native PAGE verifying the B-walker movement. Electrochemical characterization of the stepwise electrode modification process: (D) CV and (E) EIS of (a) bare GCE, (b) CdS/GCE, (c) H-DNT/CdS/GCE, and (d) H2/H-DNT/CdS/GCE. The measurement was carried out in 0.1 M PBS (pH 7.4) containing 5.0 mM $[Fe(CN)_6]^{3-/4-}$ and 0.1 M KCl at a scan rate of 100 mV s^{-1}.

across the interface leads to signal amplification through repeated hybridization−displacement cycles, which is a robust strategy for high-sensitivity miRNA detection, representing a new design paradigm for DNA walker-based biosensing systems.

3.2. Characterization of the Prepared Nanomaterials.

The morphology of the synthesized DNA nanotubes (H-DNT) and CdS QDs was characterized using atomic force microscopy (AFM) and transmission electron microscopy (TEM). The influence of annealing time on nanotube formation was systematically evaluated (Figure S3), and optimal conditions were determined. As shown in AFM images (Figure 1A,B), the assembled DNA nanotubes had well-defined, linear structures extending several micrometers in length. Cross-sectional height analysis (Figure 1C) revealed that the average height was 2.5 nm, which is much lower than the theoretical 10 nm, likely due to flattening during drying on the mica substrate and compression by the AFM tip.[31−33] This corresponds to the expected bilayer height (∼2.8 nm), which is twice the diameter of double-stranded DNA (1.4 nm). Further structural validation via agarose gel electrophoresis (Figure S4) showed that the migration of the H-DNT sample (lane 10) was significantly slower than the single-stranded controls (lanes 1−9), which confirms the formation of higher molecular weight nanotube assemblies. To verify the successful assembly of the track structure, a biotin−streptavidin indirect labeling strategy was employed (Figure S5). AFM images demonstrated uniform distribution of streptavidin on the nanotube surface with an approximate 4 nm height increase, confirming the precise formation of the predetermined architecture.

TEM analysis (Figure 1D) showed that the synthesized CdS QDs were monodispersed with a uniform particle size distribution. Their average diameter, calculated by Gaussian fitting of the particle size histogram (Figure S6A) was 3.6 nm. High-resolution TEM (HRTEM) images revealed clear lattice fringes with an interplanar spacing of 2.45 Å, consistent with the (102) crystallographic plane of hexagonal CdS (JCPDS no. 89-0440).[34] To further determine the phase of the nanoparticles, we performed X-ray diffraction (XRD) analysis (Figure S6B), which confirms that the CdS QDs were successfully synthesized. AFM characterization (Figure 1E) further supported these findings, showing that the average height was 2.1 nm, which is consistent with the expected particle size. Despite their relatively weak absorption near 365 nm, the CdS QDs were able to generate strong and stable ECL signals (Figure 1F). Stability assessments under physiological conditions demonstrated the QDs had excellent reproducibility during 25 consecutive cycles (RSD = 1.2%, Figure S7A) and high long-term performance after 7 days of storage (Figure S7B). These results show that the developed CdS QDs have high structural and electrochemical stability, which are the characteristics essential for their role in biosensing applications.

3.3. Characterization of Sensing Platform.

Polyacrylamide gel electrophoresis (PAGE) was used to verify the proposed strand displacement-mediated amplification mechanism and B-walker activation process. In Figure 2A, lanes 1−5 represent individual components: ST, AP, FS, TG, and miRNA-221, respectively. Hybridization of ST with FS (lane 6) resulted in a band shift toward slower mobility, which confirms the formation of a duplex structure. The electrophoretic mobility of the ternary mixture of ST/AP/TG (lane

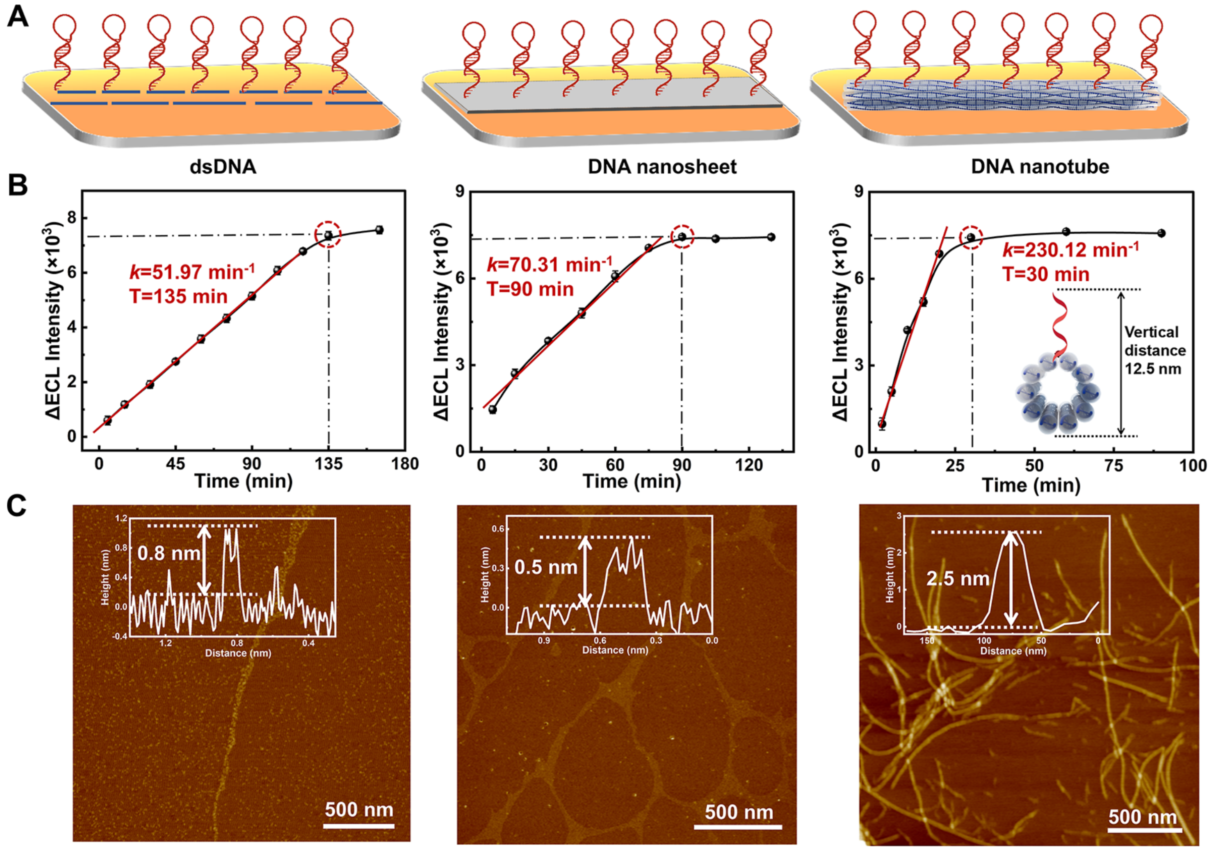

Figure 3. Performance comparison and structural characterization of three track types for the B-walker system. (A) Schematic diagrams of different track types: dsDNA, DNA nanosheet, and DNA nanotube. (B) Reaction kinetics of the three track types in the presence of 1 fM miRNA-221. (C) AFM images of the three track types.

7) further decreased, indicative of triplex T1 formation. The introduction of miRNA-221 (lane 8) caused the T1 band to weaken and a new band corresponding to free AP to appear, indicative of miRNA-triggered displacement and generation of T2. The addition of FS (lane 9) led to the disappearance of the T2 band, an indication of miRNA-221 recycling and TG strand release. No detectable band was observed in the negative control (lane 10), confirming that the system has high specificity toward the target miRNA.

Figure 2B further confirms the successful construction and activation of the B-walker. Lane 1 shows a sharp single band of Probe A, suggesting its high purity. Hybridization of Probe A with Probe B (lane 3) produced a new band with reduced mobility, confirming the formation of the B-walker complex. A band in lane 4 was further shifted due to the introduction of the assist strand, which is indicative of the locked conformation of the B-walker. In lane 5, the addition of the TG strand to the locked complex resulted in the appearance of four distinct bands, including a low-mobility band of the TG-assist duplex (as observed in lane 2). This result confirms that TG effectively displaced the assist strand and reactivated the B-walker via competitive strand displacement.

To validate the dynamic movement and strand exchange ability of the B-walker on the electrode interface, PAGE assays were performed (Figure 2C). Lanes 1 and 2 show individual bands of the hairpin probes H1 and H2, respectively. Additional faint bands were observed in the annealed mixture (lane 3), indicating that their spontaneous hybridization was minimal. In contrast, a distinct band with a slower migration rate was observed in the H1/H2 mixture (lane 4), confirming that the hybridization was highly efficient. Lane 5 shows a band of the B-walker alone, while lane 6 (B-walker + H1) exhibits a significantly retarded band, which is indicative of successful hybridization. In the ternary system (lane 7), the appearance of the H1−H2 duplex band confirms that H2 can displace H1 from the B-walker complex via strand exchange, thereby releasing the walker to continue its catalytic cycle.

Stepwise construction of the sensor interface was evaluated using cyclic voltammetry (CV) and electrochemical impedance spectroscopy (EIS). As shown in Figure 2D, the bare glassy carbon electrode (GCE, curve a) exhibited well-defined and reversible redox peaks, indicative of fast electron transfer. After modification with CdS QDs (curve b), the redox current decreased, due to the insulating effect of the Nafion-protected semiconductor layer. Subsequent immobilization of H-DNT tracks (curve c) further suppressed the redox signal due to electrostatic repulsion between the negatively charged DNA backbone and the $[Fe(CN)_6]^{3-/4-}$ redox couple, which confirms the successful DNA anchoring. Upon incubation with the B-walker and ferrocene-labeled H2 probes (curve d), the current further decreased due to the accumulation of Fc-labeled DNA at the electrode interface. This provides direct evidence for B-walker migration along the H-DNT track. EIS analysis (Figure 2E) revealed consistent trends: CdS modification led to a marked increase in charge transfer resistance (Ret, curve b), and subsequent H-DNT immobilization (curve c) and B-walker integration elevated Ret values.

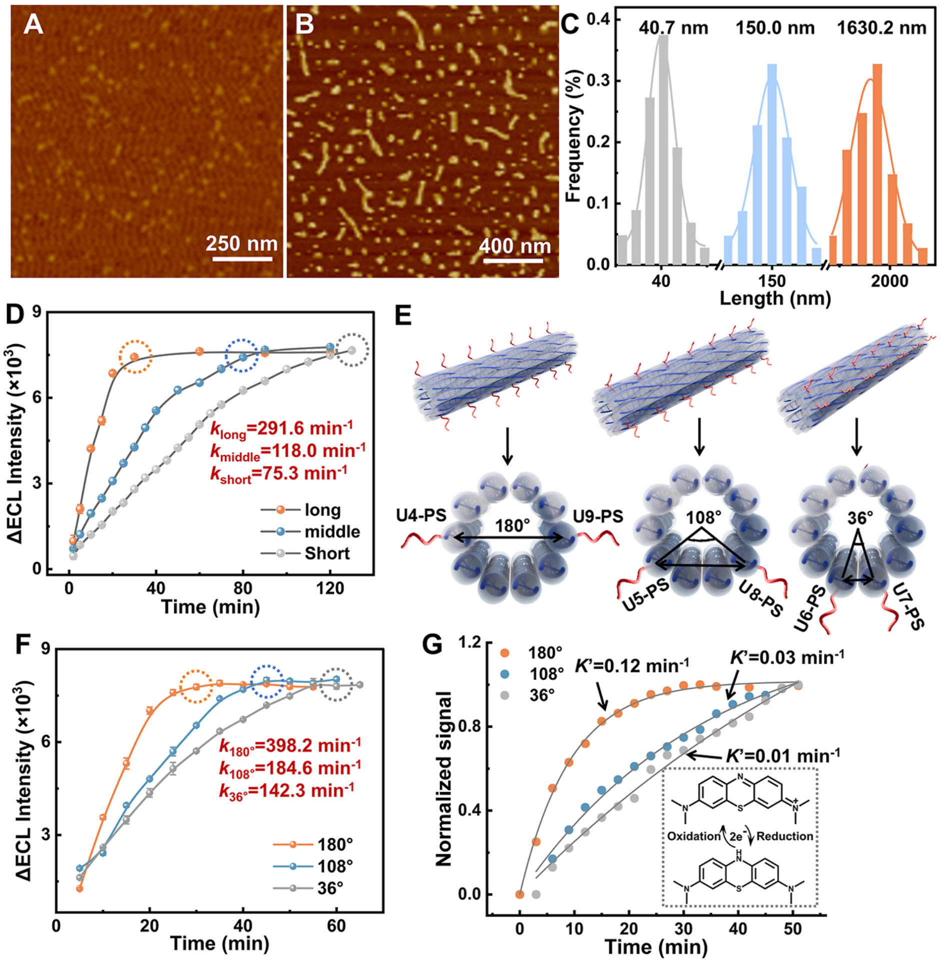

Figure 4. Effects of nanotube length and intertrack angle on reaction kinetics. (A) AFM topography image of short DNA nanotubes (40 nm). (B) AFM topography image of medium DNA nanotubes (150 nm). (C) Length distribution of DNA nanotubes with lengths of 40 nm, 150 nm, and 1.6 *μ*m. (D) Reaction kinetics of nanotube systems with varying lengths. (E) 3D (top) and cross-sectional (bottom) schematic diagrams of double-track DNA nanotubes with dihedral angles of 180°, 108°, and 36° respectively. (F) Effect of intertrack angle on reaction kinetics. (G) Correlation between track angles and hybridization kinetics.

These changes confirm the successful layer-by-layer assembly of each functional component on the electrode surface.

Fc-labeled H2 probes serve as the driving elements for B-walker activation, while playing a crucial role in controlling signal output. Their accumulation at the electrode interface leads to ECL signal quenching. To find optimal conditions, we systematically investigated the effects of probe concentration and incubation time on the system performance. As shown in Figure S8A, ECL intensity decreased progressively with increasing H2 concentration from 1 to 5 *μ*M until reaching a plateau at 2 *μ*M. Therefore, 2 *μ*M was selected as the optimal concentration for H2 immobilization. Time-course analysis (Figure S8B) revealed that ECL intensity followed the characteristic rise and fall trend, with maximum performance observed at 40 min, which was considered the optimal reaction time.

3.4. Comparative Analysis of Track Types. Track design plays a pivotal role in determining DNA walker kinetics, as mechanical rigidity and binding interface uniformity critically influence walking efficiency.[35,36] To evaluate the dimensional effects on track kinetics, we systematically compared time-resolved ECL responses of three distinct DNA frameworks, including double-stranded DNA (dsDNA), DNA nanosheets, and DNA nanotubes, each carrying identical hairpin probes spaced at 7 nm apart (Figure 3A). As shown in Figure 3B, dsDNA-based tracks required 135 min to reach ECL equilibrium, which corresponds to a walking rate constant (k) depending on the slope of ECL intensity−time curve was 51.97 min^{-1}. DNA nanosheet-based tracks had higher performance, with the equilibration time reduced to 90 min and the walking rate increased to 70.31 min^{-1}. In contrast, the DNA nanotube-based system reached equilibrium in only 30 min, with a remarkably higher rate constant of 230.12 min^{-1}, which is a 4.4-fold increase compared to dsDNA tracks. AFM images (Figure 3C) revealed the underlying structural differences underlying this performance gradient. All three structures exhibit micrometer-scale lengths, but AFM measurements reveal that both ds DNA and DNA nanosheets have a vertical height of less than 1 nm. This structural feature induces significant steric hindrance when approaching the electrode surface, thereby severely impeding the efficient strand displacement of DNA.[37] In contrast, the DNA nanotube system combined extended track length, periodic rigidity, and elevated spatial separation from the electrode, allowing for highly efficient, directed walker migration and signal transduction. These findings show that the DNA nanotubes can be used as molecular scaffolds for high-speed, programmable biosensing.

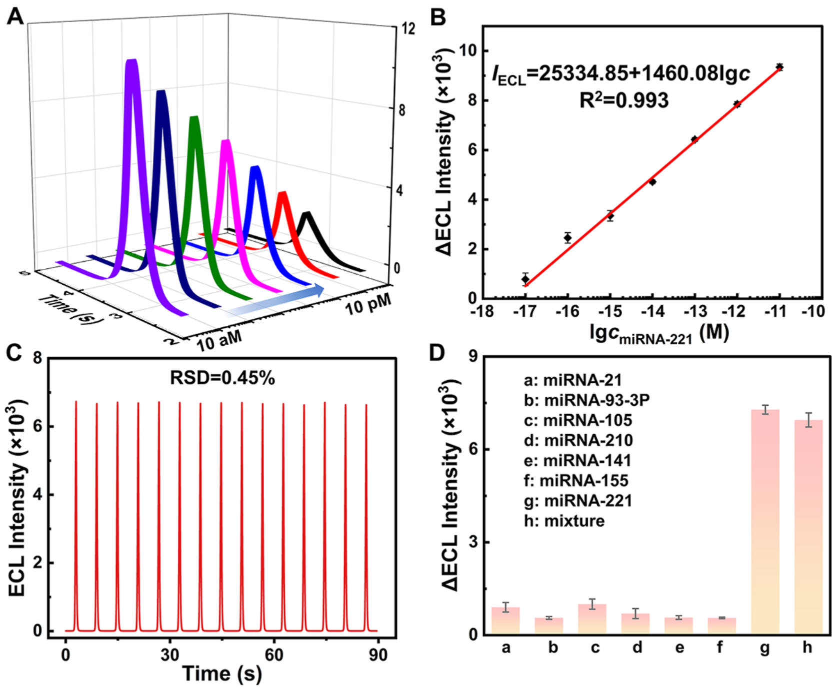

Figure 5. Performance evaluation of the DNA Walker-based miRNA-221 detection. Concentration-dependent ECL responses of the biosensor to miRNA-221: (A) ECL intensity versus miRNA-221 concentrations (10^{-11} to 10^{-17} mol/L), and (B) linear relationship between ECL signals and log $C_{\text{miRNA-221}}$. (C) Stability of the biosensing platform. (D) Specificity of the developed sensor system.

Together, these results highlight the influence of dimensional design on DNA walker performance. By integrating rigidity at the nanoscale, long-range continuity, and spatially optimized probe presentation, the DNA nanotube track can overcome key limitations of conventional planar and linear substrates.[38] Notably, the high walking velocity and short equilibrium time of the nanotube tracks allowed for rapid signal amplification and efficient target detection, which are properties essential for time-sensitive biosensing applications. This dimensional advantage was evident in miRNA-221 detection, in which the nanotube-based system was able to deliver ECL responses within 30 min. These findings underscore the importance of rational framework engineering in the development of advanced DNA walker platforms and lay a foundation for the subsequent exploration of tracks with tunable parameters such as length and intertrack spacing.

3.5. Regulation of Biosensing Ability by H-DNT. To investigate the effect of track length on DNA walker performance, we synthesized a series of rigid DNA nanotubes (H-DNTs) with precisely defined lengths (40.7 nm, 150.0 nm, and 1.63 μm), as confirmed by AFM imaging (Figure 4A–C). Time-resolved ECL analysis (Figure 4D) revealed a strong correlation between track length and biosensing kinetics. Short H-DNTs (40.7 nm) required 125 min to reach equilibrium, and their calculated walking rate constant was 75.3 min^{-1}. Increasing the track length to 150 nm reduced the equilibration time to 80 min and increased the walking rate constant to 118.0 min^{-1}. Notably, the 1.63 μm H-DNT exhibited the highest performance, achieve equilibrium in just 30 min the extended, continuous framework minimized derailment events and significantly enhanced both the walking rates and signal amplification.[7,39] These results highlight the critical role of structural continuity in optimizing walker-driven signal transduction.

To further modulate biosensing kinetics, we examined the influence of intertrack spacing in dual-track H-DNT systems by varying the dihedral angle between adjacent tracks (36°, 108°, and 180°; Figure 4E). We found that tighter configurations (36°) exhibited slower ECL response, requiring 55 min to reach equilibrium with a walking rate of 142.3 min^{-1} (Figure 4F). Increasing the angle to 108° accelerated hybridization, reducing the equilibration time to 45 min, and increasing the walking rate to 184.6 min^{-1}. The most efficient performance was observed at 180°, where the system reached equilibrium within only 25 min and achieved a rate constant of 398.2 min^{-1}. These results indicate that increasing intertrack distance can mitigate lateral steric hindrance, thereby enhancing probe accessibility and improving hybridization efficiency.[40]

To further validate the effect of intertrack spacing on hybridization dynamics, we employed methylene blue (MB)-labeled complementary DNA as a redox probe and monitored hybridization kinetics in real time using square wave voltammetry (SWV; Figures 4G and S9). The system with a 36° dual-track configuration had slow signal accumulation, reaching saturation at ~50 min. The 108° configuration reached saturation within 40 min, indicative of enhanced kinetics. Pseudo-first-order rate constant analysis (k') revealed a direct correlation between probe spacing and hybridization efficiency. Densely packed tracks had a low rate of 0.01 min^{-1}, whereas those with high angle (180°) had a high k' of 0.12 min^{-1}, which is a 12-fold increase. These findings suggest that larger intertrack angles improve probe accessibility and facilitate target binding at the electrode interface.

3.6. Analytical Performance of the Biosensing Platform. Following systematic optimization of assay conditions, we evaluated the performance of the biosensing platform in detecting miRNA-221. As shown in Figure 5A, the ECL intensity decreased with increasing miRNA-221 levels from 10

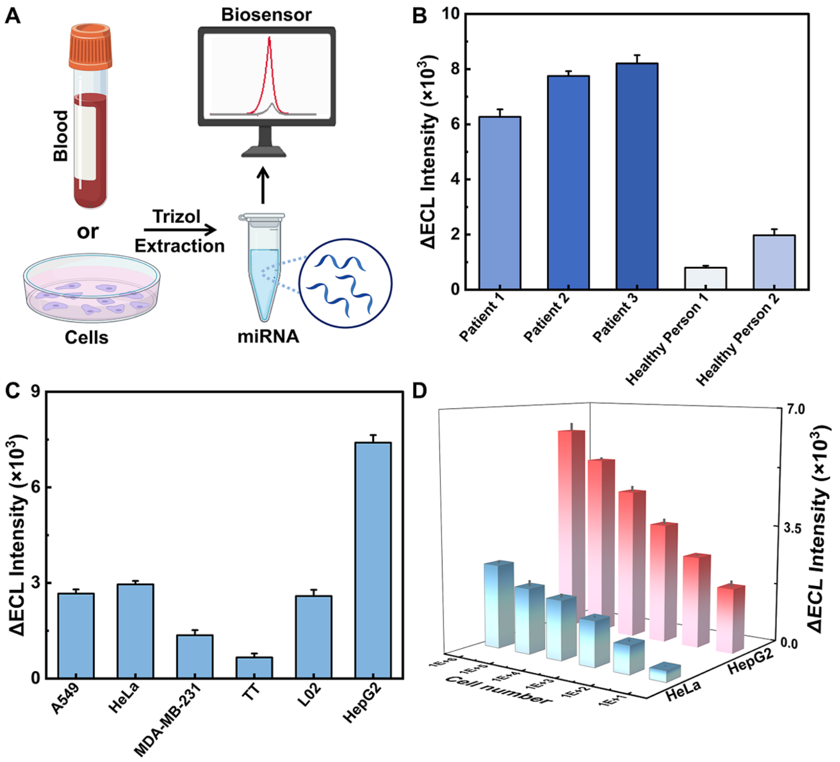

Figure 6. Applications of the biosensor in serum and cells. (A) Applications of the biosensor in serum and cells. (B) The constructed biosensor was used to detect miR-221 in serum samples from both patients and healthy individuals. (C) ECL quenching by miR-221 in different cancer cells. (D) ECL response signals of the sensor during the detection of HepG2 and HeLa cell lysates at varying concentrations (10 to 10^5 cells).

aM to 10 pM. Quantitative analysis (Figure 5B) revealed a strong linear relationship between signal intensity and the logarithm of target concentration ($I = 25334.85 + 1460.08 \lg C_{\text{miRNA-221}}$, $R^2 = 0.993$). The calculated limit of detection (LOD) was 2.42 aM (based on 3 Sb/m), Compared with the previously reported methods for detecting miRNA (Table S2), this work demonstrates a lower detection limit. The sensor also had excellent repeatability, with a relative standard deviation (RSD) of only 0.45% over 15 repeated measurements of 10 fM samples (Figure 5C). Intra-assay precision was evaluated by analyzing eight replicate biosensors containing 1 fM miRNA-221 prepared in the same batch (Figure S10A). The detection system demonstrated excellent reproducibility with a relative standard deviation (RSD) of only 1.2%. Significantly, the ECL intensity retained 86.5% of its initial value after 7 days (Figure S10B), manifesting an acceptable stability of this proposed sensing platform. Specificity analysis confirmed its high selectivity: only miRNA-221 and its mixture generated strong signals, while structurally similar sequences (e.g., miRNA-21, miRNA-93-3p) elicited negligible responses (Figure 5D). These results collectively demonstrate that the developed platform has ultrahigh sensitivity, exceptional reproducibility, and strong sequence specificity, positioning it as a robust tool for miRNA biomarker analysis.

3.7. Application of the Proposed Biosensor in Actual Samples. Blood samples were collected from multiple hepatocellular carcinoma (HCC) patients, and miRNAs were extracted using the Trizol lysis method for analysis. The detection results demonstrated that only trace amounts of miR-221 were present in healthy control, whereas HCC patients exhibited significantly elevated miR-221 expression levels (Figure 6B). Clinical correlation suggested that Patient 3 had higher tumor staging compared to other patients. To validate the clinical applicability of this detection platform, we further analyzed miR-221 expression across various cancer cell lines, including thyroid carcinoma (A549), cervical carcinoma (HeLa), breast cancer (MDA-MB-231), medullary thyroid carcinoma (TT), normal hepatocytes (L02), and hepatocellular carcinoma (HepG2). As shown in Figure 6C, differential miR-221 expression levels among cell lines induced varying degrees of ECL signal quenching. Although statistical analysis confirmed miR-221 expression in all tested cancer cells, HepG2 cells displayed remarkably higher miR-221 expression compared to other cancer types. Based on this significant difference, we selected HepG2, which exhibited the most pronounced miR-221 expression signature, and HeLa with relatively low expression levels for subsequent comparative analysis. As illustrated in Figure 6D, the ECL signal of HepG2 samples decreased progressively with increasing cell numbers (10 to 10^5), an indication of elevated miRNA-221 levels. In contrast, HeLa cells exhibited minimal signal variation, indicative of low miRNA-221 expression. These distinct profiles align with known differences between the two cell lines and validate the sensor's capacity to accurately quantify miRNA in complex cellular matrices. This distinctive expression pattern enables our biosensor to achieve highly specific identification of hepatocellular carcinoma cells.

To further evaluate the applicability of the method in clinical diagnostics, we conducted recovery experiments in human serum using the standard addition method. A series of miRNA-221 standards were spiked into 100-fold diluted serum from healthy donors. The ECL intensities were converted to concentrations using the calibration curve, and recovery rates were calculated (Table S3). All recovery rates ranged from 93.0% to 104.9%, confirming the accuracy and suitability of the method in the quantitative detection of miRNA-221 in real biological samples.

4. CONCLUSIONS

In summary, we developed a programmable, micrometer-scale DNA nanotube (H-DNT)-based platform containing periodically spaced anchoring sites that serve as directional tracks for bipedal DNA walkers. This structural innovation was further used to construct a high-performance electrochemical biosensor for miRNA-221 detection. The system offers two key advantages: (1) the rigidity and periodicity of the nanotube architecture provide stable binding interfaces that enhance walker path fidelity and molecular recognition efficiency; and (2) the extended, ordered structure supports continuous, directional walker movement and significantly improves kinetic performance and signal amplification. This modular strategy not only overcomes the size and structural limitations of conventional DNA assemblies but also enhances the functional versatility of DNA-based nanomachines. The platform holds strong potential for future applications in intelligent diagnostics, precision medicine, and programmable biosensors.

■ ASSOCIATED CONTENT

Supporting Information

The Supporting Information is available free of charge at https://pubs.acs.org/doi/10.1021/acs.analchem.5c05240.

> Additional experimental details include reagents, apparatus, DNA oligonucleotide sequence information, synthesis of dsDNA and DNA nanosheet, AFM characterization, PAGE analysis of the sensing strategy, supporting characterization of CdS QDs, supporting tables (PDF)

■ AUTHOR INFORMATION

Corresponding Authors

Pinyi Ma − *College of Chemistry, Jilin Province Research Center for Engineering and Technology of Spectral Analytical Instruments, Jilin University, Changchun 130012, China;* orcid.org/0000-0002-3230-4928; Email: mapinyi@jlu.edu.cn

Daqian Song − *College of Chemistry, Jilin Province Research Center for Engineering and Technology of Spectral Analytical Instruments, Jilin University, Changchun 130012, China;* orcid.org/0000-0002-4866-1292; Email: songdq@jlu.edu.cn

Authors

Yongli Wu − *College of Chemistry, Jilin Province Research Center for Engineering and Technology of Spectral Analytical Instruments, Jilin University, Changchun 130012, China*

Xin Chang − *Department of Breast Surgery, The Second Hospital of Jilin University, Changchun 130041, China*

Zhuoxin Ye − *College of Chemistry, Jilin Province Research Center for Engineering and Technology of Spectral Analytical Instruments, Jilin University, Changchun 130012, China*

Ruixin Liu − *College of Chemistry, Jilin Province Research Center for Engineering and Technology of Spectral Analytical Instruments, Jilin University, Changchun 130012, China*

Yan Zhang − *College of Chemistry, Jilin Province Research Center for Engineering and Technology of Spectral Analytical Instruments, Jilin University, Changchun 130012, China*

Ruiyan Liu − *College of Chemistry, Jilin Province Research Center for Engineering and Technology of Spectral Analytical Instruments, Jilin University, Changchun 130012, China*

Complete contact information is available at:
https://pubs.acs.org/10.1021/acs.analchem.5c05240

Notes

The authors declare no competing financial interest.

■ ACKNOWLEDGMENTS

This work was supported by the National Natural Science Foundation of China (22074052 and 22004046), the Science and Technology Developing Foundation of Jilin Province of China (20230101033JC), and the Jilin Provincial Department of Education Program for Enhancing Ph.D. Students' Scientific Research and Innovation Capabilities (JJKH20250064BS).

■ REFERENCES

(1) Jung, C.; Allen, P. B.; Ellington, A. D. *Nat. Nanotechnol.* **2016**, *11*, 157−163.

(2) Yao, D.; Bhadra, S.; Xiong, E.; Liang, H.; Ellington, A. D.; Jung, C. *ACS Nano* **2020**, *14*, 4007−4013.

(3) Wang, L.; Liu, P.; Liu, Z.; Zhao, K.; Ye, S.; Liang, G.; Zhu, J.-J. *ACS Sens.* **2020**, *5*, 3584−3590.

(4) Li, C.-Y.; Liu, J.-X.; Yuheng, L.; Gao, J.-L.; Chen, Y.-L.; He, J.-W.; Xin, M.-K.; Liu, D.; Zheng, B.; Sun, X. *Anal. Chem.* **2022**, *94*, 5450−5459.

(5) Thubagere, A. J.; Li, W.; Johnson, R. F.; Chen, Z.; Doroudi, S.; Lee, Y. L.; Izatt, G.; Wittman, S.; Srinivas, N.; Woods, D.; Winfree, E.; Qian, L. *Science* **2017**, *357*, No. eaan6558.

(6) Gao, Y.; Fan, X.; Zhang, X.; Guan, Q.; Xing, Y.; Song, W.; Song, D. *Anal. Chem.* **2025**, *97*, 2402−2410.

(7) Yao, T.; Kong, L.; Liu, Y.; Li, H.; Yuan, R.; Chai, Y. *Anal. Chem.* **2022**, *94*, 12256−12262.

(8) Yang, H.; Shen, H.; Qileng, A.; Cui, G.; Liang, Z.; Liu, Y.; Liu, W. *Anal. Chem.* **2023**, *95*, 5764−5772.

(9) Chao, J.; Wang, J.; Wang, F.; Ouyang, X.; Kopperger, E.; Liu, H.; Li, Q.; Shi, J.; Wang, L.; Hu, J.; Wang, L.; Huang, W.; Simmel, F. C.; Fan, C. *Nat. Mater.* **2019**, *18*, 273−279.

(10) Yin, P.; Choi, H. M. T.; Calvert, C. R.; Pierce, N. A. *Nature* **2008**, *451*, 318−322.

(11) Ogieva, M. O.; Pfeifer, W. G.; Sensale, S. *Sci. Rep.* **2025**, *15*, 9450.

(12) Lin, M.; Wang, J.; Zhou, G.; Wang, J.; Wu, N.; Lu, J.; Gao, J.; Chen, X.; Shi, J.; Zuo, X.; Fan, C. *Angew. Chem., Int. Ed.* **2015**, *54*, 2151−2155.

(13) Hariadi, R. F.; Sommese, R. F.; Adhikari, A. S.; Taylor, R. E.; Sutton, S.; Spudich, J. A.; Sivaramakrishnan, S. *Nat. Nanotechnol.* **2015**, *10*, 696−700.

(14) Ge, Z.; Gu, H.; Li, Q.; Fan, C. *J. Am. Chem. Soc.* **2018**, *140*, 17808−17819.

(15) Goodman, R. P.; Schaap, I. A. T.; Tardin, C. F.; Erben, C. M.; Berry, R. M.; Schmidt, C. F.; Turberfield, A. J. *Science* **2005**, *310*, 1661−1665.

(16) Pan, M.-C.; Gao, M.-H.; Yang, X.; Liang, W.-B.; Yuan, R.; Zhuo, Y. *ACS Sens.* **2022**, *7*, 2475−2482.

(17) Yao, T.; Chen, J.; Kong, L.; Liu, Y.; Yuan, R.; Chai, Y. *Anal. Chem.* **2023**, *95*, 13211−13219.

(18) Ibusuki, R.; Morishita, T.; Furuta, A.; Nakayama, S.; Yoshio, M.; Kojima, H.; Oiwa, K.; Furuta, K. y. *Science* **2022**, *375*, 1159−1164.

(19) Wickham, S. F. J.; Endo, M.; Katsuda, Y.; Hidaka, K.; Bath, J.; Sugiyama, H.; Turberfield, A. J. *Nat. Nanotechnol.* **2011**, *6*, 166−169.

(20) Ye, Z.; Ma, M.; Chen, Y.; Yang, J.; Zhao, C.; Diao, Q.; Ma, P.; Song, D. *Anal. Chem.* **2024**, *96*, 17984−17992.

(21) Falahi, S.; Rafiee-Pour, H.-A.; Zarejousheghani, M.; Rahimi, P.; Joseph, Y. *Biomedicines* **2021**, *9*, 964.

(22) Lei, Y.; Fei, X.; Ding, Y.; Zhang, J.; Zhang, G.; Dong, L.; Song, J.; Zhuo, Y.; Xue, W.; Zhang, P.; Yang, C. *Sci. Adv.* **2023**, *9*, No. eadi1556.

(23) Zhang, P.; Wang, C.; Zhao, J.; Xiao, A.; Shen, Q.; Li, L.; Li, J.; Zhang, J.; Min, Q.; Chen, J.; Chen, H.-Y.; Zhu, J.-J. *ACS Nano* **2016**, *10*, 3637−3647.

(24) Liu, W.; Liao, N.; Lei, Y.; Liang, W.; Yang, X.; Yuan, R.; Yang, C.; Zhuo, Y. *Adv. Sci.* **2024**, *11*, 2401253.

(25) Zhou, Q.; Li, T.; Li, X.; Wei, L.; Luo, J.; Bai, L.; Duan, W.-J.; Xie, B.; Sun, B.; Chen, J.-X.; Dai, Z.; Chen, J. *Anal. Chem.* **2024**, *96*, 6774−6783.

(26) Zhou, X.; Geng, H.; Shi, P.; Wang, H.; Zhang, G.; Cui, Z.; Lv, S.; Bi, S. *Biosens. Bioelectron.* **2024**, *247*, 115916.

(27) Karakatsanis, A.; Papaconstantinou, I.; Gazouli, M.; Lyberopoulou, A.; Polymeneas, G.; Voros, D. *Mol. Carcinog.* **2013**, *52*, 297−303.

(28) Qi, M.-Y.; Conte, M.; Tang, Z.-R.; Xu, Y.-J. *ACS Nano* **2022**, *16*, 17444−17453.

(29) Yin, P.; Hariadi, R. F.; Sahu, S.; Choi, H. M. T.; Park, S. H.; LaBean, T. H.; Reif, J. H. *Science* **2008**, *321*, 824−826.

(30) Wilner, O. I.; Orbach, R.; Henning, A.; Teller, C.; Yehezkeli, O.; Mertig, M.; Harries, D.; Willner, I. *Nat. Commun.* **2011**, *2*, 540.

(31) Stewart, J. M.; Geary, C.; Franco, E. *ACS Nano* **2019**, *13*, 5214−5221.

(32) Xu, F.; Wu, T.; Shi, X.; Pan, L. *Nanotechnology* **2019**, *30*, 115602.

(33) Xie, Y.; Xie, X.; Lv, H.; Dai, Z.; Chen, X.; Gao, Z.; Xu, L.; Li, J.; Wang, F.; Fan, C.; Li, Q. *Nano Lett.* **2025**, *25*, 9302−9310.

(34) Ge, F.; Zhao, Y.; Feng, C.; Li, X.; Wang, J.; Liu, H.; Hu, L.; Chen, Y.; Chen, F.; Cheng, F.; Wei, H.-Y.; Wu, X.-J. *ACS Appl. Mater. Interfaces* **2024**, *16*, 32847−32856.

(35) Schlapak, R.; Danzberger, J.; Armitage, D.; Morgan, D.; Ebner, A.; Hinterdorfer, P.; Pollheimer, P.; Gruber, H. J.; Schäffler, F.; Howorka, S. *Small* **2012**, *8*, 89−97.

(36) Li, M.; Song, L.; Liu, M.; Guo, R.; Lin, M.; Zuo, X. *ACS Nano* **2025**, *19*, 23142−23150.

(37) Mahshid, S. S.; Vallée-Bélisle, A.; Kelley, S. O. *Anal. Chem.* **2017**, *89*, 9751−9757.

(38) Platnich, C. M.; Hariri, A. A.; Rahbani, J. F.; Gordon, J. B.; Sleiman, H. F.; Cosa, G. *ACS Nano* **2018**, *12*, 12836−12846.

(39) Valero, J.; Famulok, M. *Angew. Chem., Int. Ed.* **2020**, *59*, 16366−16370.

(40) Pei, H.; Li, F.; Wan, Y.; Wei, M.; Liu, H.; Su, Y.; Chen, N.; Huang, Q.; Fan, C. *J. Am. Chem. Soc.* **2012**, *134*, 11876−11879.